Available online at www.sciencedirect.com
ScienceDirect
Journal of Power Sources 163 (2007) 874–881
JOURNAL OF POWER SOURCES
www.elsevier.com/locate/jpowsour

Influence of clamping force on the performance of PEMFCs

P. Zhou, C.W. Wu *, G.J. Ma

State Key Laboratory of Structure Analysis for Industrial Equipment, Department of Engineering Mechanics, Dalian University of Technology, Dalian 116024, China

Received 29 July 2006; received in revised form 28 September 2006; accepted 29 September 2006
Available online 13 November 2006

Abstract

The objective of the present paper is to investigate the effect of clamping force on the performance of proton exchange membrane fuel cell (PEMFC) with interdigitated gas distributors considering the interfacial contact resistance, the non-uniform porosity distribution of the gas diffusion layer (GDL) and the GDL deformation. The clamping force between the GDL and the bipolar plate is one of the important factors to affect the performance and efficiency of the fuel cell system. It directly affects the structure deformation of the GDL and the interfacial contact electrical resistance, and in turn influences the reactant transport and Ohmic overpotential in the GDL. Finite element method and finite volume method are used, respectively, to study the elastic deformation of the GDL and the mass transport of the reactants and products. It is found that there exists an optimal clamping force to obtain the highest power density for the PEMFC with the interdigitated gas distributors.

Keywords: Fuel cells; Contact resistance; Diffusion layer; Clamping force

1. Introduction

The proton exchange membrane fuel cell (PEMFC) system is considered as an alternative power source for electric vehicles by virtual of its high-energy efficiency, pollution-free characteristic, and simplicity in design and operation. It has received more and more attention in the world during the last decade. Numerical and experimental studies have been rapidly increased in order to improve the performance and cost-effectiveness. Experimental results have shown that a suitable design of the interdigitated flow field gives rise to a great improvement of the system performance [1]. The improvement is attributed to the fact that it converts the transport of the reactants and products in the porous electrode from a diffusion mechanism to a forced convection mechanism. Furthermore, the shear force exerted by the gas flow helps to remove most of the liquid water from the porous electrode, thereby minimizes the possibility of the electrode flooding.

Several attempts of mathematical modeling have been made to understand the advantages of the interdigitated flow field design. Yi and Nguyen [2] presented a multi-component model of the hydrodynamics of the reactant gas in the porous electrode of the PEMFC with the new design flow field. This model was then extended to the two dimensional and two-phase multi-component transport model by He et al. [3] to account for the effects of liquid water in the porous electrode on the PEMFC performance. They investigated the effects of the operating conditions and the design parameters of the air cathode on the performance of the fuel cell. The study indicates that the saturation of liquid water at the cathode greatly affects the system performance and efficiency. Using the similar model, Wang et al. [4,5] investigated effects of the magnetic particles on the performance of the PEMFC with the interdigitated gas distributors. All the models mentioned above have assumed for simplicity that the porosity of the GDL is constant, i.e., the GDL is assumed to be a rigid material whose porosity is independent of the camping force.

In order to seal the fuel cell against any gas leakages and reduce the interfacial contact resistance, the gas diffusion layers and the bipolar plates are usually bolted together under a suitable pressure, as shown in Fig. 1. Obviously, the pressure will reduce the porosity below the shoulder area, which in turn increases the convection resistance of the reactants and products. The experimental observation [7] has shown that the clamping force will strongly affect the power density of PEMFCs. Roshandel et al. [8] investigated the fuel cell performance considering the effects

* Corresponding author. Tel.: +86 411 84706353; fax: +86 411 84706353.
E-mail address: cwwu@dlut.edu.cn (C.W. Wu).

0378-7753/$ – see front matter © 2006 Elsevier B.V. All rights reserved.
doi:10.1016/j.jpowsour.2006.09.068

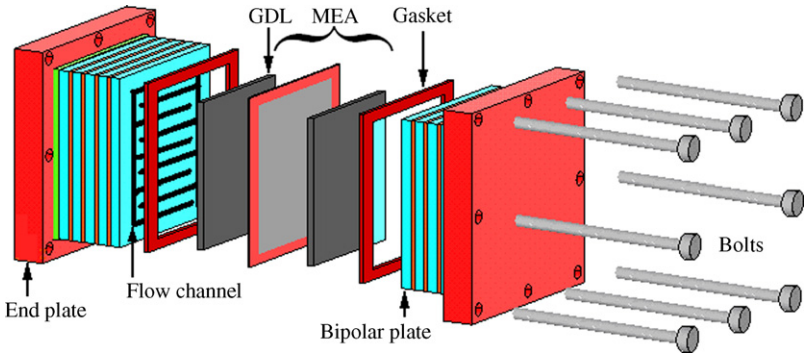

Fig. 1. Schematic of a PEM fuel cell stack.

of porosity variation in the GDL. Their numerical analysis show that a decrease in the porosity reduces the reactant transport in the GDL. Chu et al. [9] investigated effects of the non-uniform porosity caused by liquid water on the fuel cell performance in terms of some representative parameters, such as oxygen consumption, power density, etc. The non-uniformity of the porosity in the GDL is supposed to be described by four different continuous functions of the coordinate position. However, all of those models considering the non-uniformity of the porosity have assumed that the porosity varies as a simple function given previously. Zhou et al. [6] recently studied the interfacial contact resistance and elastic deformation of the GDL using finite element method, and found that the porosity distribution of the GDL strongly depends on the clamping force and the structure of the bipolar plates. It is found that the porosity distribution exists in a complex manner, but cannot be described by a simple function given previously.

The objective of the present work is to study the effects of the compression pressure due to the clamping force on the performance of PEMFC with the interdigitated gas distributors. In this work, we first use a finite element method (FEM) to analyze the contact pressure, the deformation of GDL, and the porosity distribution, then we analyze the mass transport using a two-phase flow model. The numerical results show that a high clamping force results in a lower porosity in the GDL, which will increase the transport resistances of both the gas phase and liquid phase. On the other hand, a high clamping force may decrease the interfacial contact resistance, and hence minimize the electrical resistance loss inside the fuel cell. These two effects may work together to yield an optimum clamping force for the fuel cell.

2. Model description

The computational domain, i.e., the region surrounded by the dashed line as shown in Fig. 2a, consists of the gas diffusion layer and a period of the interdigitated gas distributor. Although the studied domain of the FEM model to analyze the GDL deformation can be half of what is adopted in the two-phase flow model considering the symmetrical characteristic of the GDL deformation, we still use the same domain as the two-phase flow model in order to easily transfer the computational data between the two models.

2.1. FEM model

The FEM analysis model, as shown in Fig. 2b, is used to analyze the elastic deformation of the GDL and the porisity destribution. It is assumed that the cathod and the anode of the bipolar plates have the same structure, and the compressive modulus of the catalyst and membrane layer (about 100 MPa, T65-RH30) [10] are much higher than that of the gas diffusion layer (∼10 MPa) [11]. Therefore, the deformation of the catalyst and membrane layer can be neglected, and will not be considered in the FEM analysis of the elastic deformation of the cell structure. Normal displacements at the left, right and bottom boundaries of the gas diffusion layer were restricted

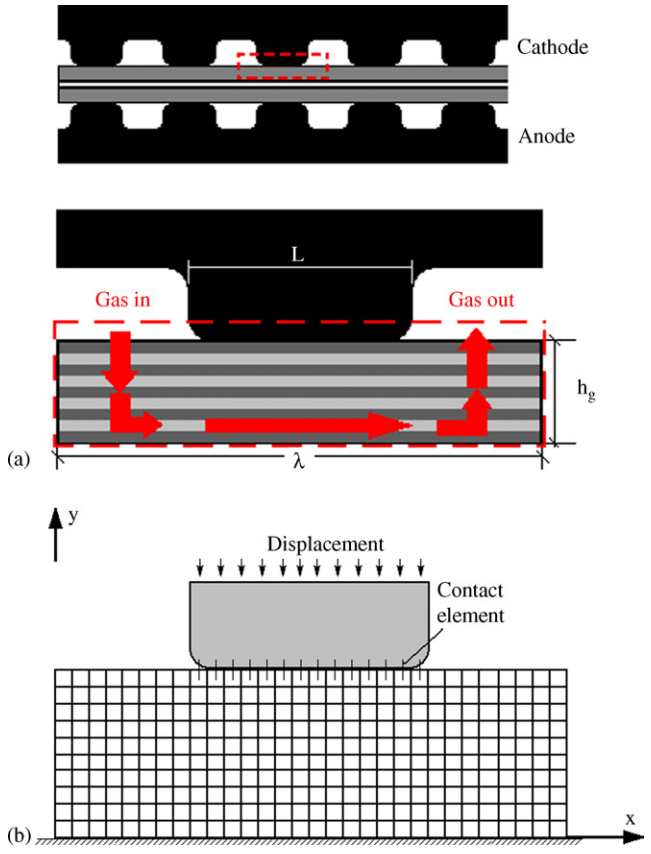

Fig. 2. A schematic of (a) electrode of polymer electrolyte membrane (PEM) fuel cell and (b) FEM analysis model.

Table 1
Parameters of the GDL used in the FEM analysis

Porosity	E_c (cross-plane) (MPa)	E_i (in-plane) (MPa)	Interfacial resistivity, ρ (mΩ cm^2)
0.7	10	100	$\rho = 2.0\ (5.0p/E_c)^{-0.7}$ for case A $\rho = 20\ (2.0p/E_c)^{-1}$ for case B

The interfacial resistivities for cases A and B are based on the experimental results using the graphite shoulder and the stainless steel shoulder, respectively [11,13,14].

due to the symmetry of the structure. Bipolar plate is treated as rigid structure. The vertical displacement of the shoulder is given downwards, simulating the stacking process. The problem mentioned above can be described as a large deformation contact problem with plane-strain boundary [12]. Plane-strain elements were used and contact elements were built at the possible contact region, as shown in Fig. 2.

We use carbon cloth or carbon paper as the GDL material. The carbon paper is a kind of non-woven paper of carbon fibres, which is an anisotropic porous material. The mechanical property of the GDL and the relationship between the contact pressure and the interficial electric resistivity should be considered to obtain the porosity distribution and total interficial resistance. However, only a few open literatures have been reported on the modeling of the mechanical performance of the GDLs and the total contact resistance between the GDL and the shoulder. The parameters employed in the present paper are given in Table 1. Most of the data are based on the experimental results and simulating models of the similar material [11,13–15]. Cases A and B are based on the experimental results using the graphite shoulder and the stainless steel shoulder, respectively. The Ohmic overpotential depends on the parameters used in the contact resistance model (see Table 1). However, we found that they will not influence the general conclusions if the model of contact resistivity does not change but the contact resistivity varies in the same order.

2.2. Porosity distribution and interficial resistance calculation

The GDL deformation and the interfacial contact pressure are first obtained using the FEM analysis. Then, the porosity distribution and interficial resistance are calculated. Based on the large deformation theory of solid mechanics [12], the porosity after stacking is:

$$\bar{\phi} = \frac{\bar{V}_p}{\bar{V}} = \frac{V_0\phi_0 - V_0(1 - e^{\varepsilon_V})}{V_0 e^{\varepsilon_V}} = \frac{\phi_0 - 1 + e^{\varepsilon_V}}{e^{\varepsilon_V}} \quad (1)$$

where V_0 is the initial total volume of the porous media, ϕ_0 the initial porosity, and ε_v the bulk strain, $\bar{V}_p$ is the pore volume. The top-bar indicates the parameters after stacking. The volume of the porous media is calculated as:

$$\bar{V} = V_0 e^{\varepsilon_v} = V_0 e^{\varepsilon_x + \varepsilon_y + \varepsilon_z} \quad (2)$$

The total interfacial contact resistance in a period of the fuel cell is [6]

$$R = 2\left(\sum_{i=1}^{n} R_i^{-1}\right)^{-1} = 2\left(\sum_{i=1}^{n} A_i/\rho_i\right)^{-1} \quad (3)$$

where R_i, A_i, and ρ_i are the resistance, contact area, resistivity of the ith contact element, respectively. This equation is based on the assumption that the contact surfaces are equipotential. Therefore, the interfacial contact resistance between the two surfaces is considered as an electric circuit in parallel connections. The factor 2 in Eq. (3) is due to the same contact resistances in the anode and cathode.

The total compression force in the unit width (z direction), F, has the following relationship with the contact stress components:

$$F = \sum_{i=1}^{n} p_n^i \vec{n} + p_\tau^i \vec{\tau} \quad (4)$$

where p_n^i is the normal contact stress component (contact pressure), p_τ^i the tangential contact stress component (friction), $\vec{n}$ and $\vec{\tau}$ are the unit vectors in normal and tangential directions of contact elements, respectively. The nominal clamping pressure, p_c, is defined as:

$$p_c = \frac{F}{\lambda} \quad (5)$$

where λ is the length of the period of the cross-section of the bipolar plate as shown in Fig. 2a.

2.3. Two-phase flow model of the cathode

The following assumptions are used in the two-phase flow model of the cathode for studying the effect of the clamping force on the performance of PEMFCs: (1) steady flow state; (2) isothermal flow; (3) laminar flow in the GDL; (4) the gas and liquid in the electrode flow as continuous phases described by Darcy's law; (5) the water is generated as liquid at the membrane and electrode interface by the oxygen reduction reaction and the net water migration from the anode. Based on the above assumptions, the continuity equations are:

$$\nabla \cdot (C^g v^g) + r_w = 0 \quad (6)$$

for the gas phase, and

$$\nabla \cdot \left(\frac{v^l \rho_w}{M_w}\right) - r_w = 0 \quad (7)$$

for the liquid phase, where C^g is the gas molar concentration, v^g the gas superficial velocity, v^l the liquid superficial velocity, r_w the interfacial mass-transfer rate of the water between the gas and liquid phases, ρ_w the water density, M_w the water molecular weight.

The momentum conservation are given in the following according to Darcy's equation:

$$v^{g} = -\left(\frac{K^{g}_{eff}}{\mu^{g}}\right)\nabla P^{g} \tag{8}$$

for the gas phase, and

$$v^{l} = -\left(\frac{K^{l}_{eff}}{\mu^{l}}\right)\nabla P^{l} \tag{9}$$

for the liquid water, where P^{g}, μ^{g} and K^{g}_{eff} are the pressure, viscosity, effective permeability of the gas, respectively. P^{l}, μ^{l} and K^{l}_{eff} are the pressure, viscosity, efficient permeability of the water, respectively.

The species conservation equations are:

$$\nabla\cdot\left(C_{O}v^{g} - D^{O}_{eff}\nabla C_{O}\right) = 0 \tag{10}$$

$$\nabla\cdot\left(C_{w}v^{g} - D^{w}_{eff}\nabla C_{w}\right) + r_{w} = 0 \tag{11}$$

for O_2 and H_2O vapour, respectively. Where D^{O}_{eff} is the effective diffusivity of oxygen, D^{w}_{eff} the effective diffusivity of water vapour, C_O the molar concentration of oxygen, and C_w the molar concentration of water vapour.

The interfacial mass-transfer rate of the water between the gas and liquid phases, r_w, can be expressed as:

$$r_{w} = k_{c}\bar{\phi}(1-s)y_{w}(RT)^{-1}\left(y_{w}P^{g} - P^{sat}_{w}\right)q + k_{v}\bar{\phi}s\rho_{w}M_{w}^{-1}\left(y_{w}P^{g} - P^{sat}_{w}\right)(1-q) \tag{12}$$

with a switch function

$$q = \frac{(1 + |y_{w}P^{g} - P^{sat}_{w}|)/(y_{w}P^{g} - P^{sat}_{w})}{2} \tag{13}$$

where $y_w = C_w/C^g$, s is the saturation of the liquid water in the pore, T the temperature (°C), R the gas constant, M_w the molecular weight of water. When the water partial pressure (y_wP^g) is greater than the water saturation pressure (P^{sat}_w), the switch function $q = 1$. Otherwise, $q = 0$.

The boundary conditions have been described in the literatures [3,16], which simulate the PEMFC with the interdigitated flow field. At the boundary where $x = 0$ or $x = \lambda$ (see Fig. 2b), the symmetry conditions are used for all the parameters, and the normal gradients of the four independent variables, P^g, C_O, C_w, and s, in governing Eqs. (6)–(13) vanish. The same boundary condition is also employed at the interface of the GDL and the shoulder of the gas distributor. At the GDL/catalyst-layer interface, it is assumed that there is no normal superficial gas velocity. The mass fluxes of oxygen and liquid water can be defined as the functions of the local current density I as follows:

$$-D^{O}_{eff}\frac{\partial C_{O}}{\partial y}\bigg|_{y=0} = \frac{I}{4F} \tag{14}$$

$$\frac{\rho_{l}}{M_{w}}v^{l}\bigg|_{y=0} = -\left(\frac{1}{2}+\alpha\right)\frac{I}{F} \tag{15}$$

The liquid water flux at the interface arises from two sources: the oxygen reduction and electro-osmosis. The parameter α, which is assumed to be constant, represents the net water transport coefficient in the membrane. The mass flux of the water vapour at the interface equals zero, i.e.,

$$-D^{w}_{eff}\frac{\partial C_{w}}{\partial y}\bigg|_{y=0} = 0 \tag{16}$$

The simplified Butler–Vollmer equation is used to describe the local current density along the catalyst-layer as a function of the oxygen concentration at the GDL/catalyst-layer interface and the activation overpotential η

$$I = I_{0}\frac{\bar{\phi}}{\phi_{0}}\frac{C_{O}}{C_{O,ref}}\exp\left(\frac{2kF\eta}{RT}\right) \tag{17}$$

where I_0 is the exchange current density, $C_{O,ref}$ the oxygen reference concentration, k the transfer coefficient of oxygen reduction reaction. The two-phase flow model described above is similar to that presented by He et al. [3]. However, at the present work, some parameters and equations are described more accurately.

In the governing equation, the effective permeability and diffusivity are both correlated with the porosity and the saturation level of the liquid water. In addition, the diffusion coefficient is a function of temperature and pressure. Tomadakis and Sotirchos [17], and Nam and Kaviany [18] numerically simulated the effective diffusivity for a random fibrous porous media, and suggested that:

$$D_{eff} = Dh(T)f\left(\bar{\phi}\right)g(s) = D\left(\frac{T}{T_{r}}\right)^{b_1}\bar{\phi}\left(\frac{\bar{\phi}-\phi_{p}}{1-\phi_{p}}\right)^{b_2}(1-s)^{b_3} \tag{18}$$

where ϕ_p is a percolation threshold, D the diffusivity at T_r when $\bar{\phi} = 1$ and $s = 0$, and b_1, b_2 and b_3 are empirical constants. b_1 is 2.334 and 1.832 for vapour water and oxygen, respectively. For porous media composed of two-dimensional, overlapping, and random fibre layers: $\phi_p = 0.11$, b_2 is 0.521 and 0.785, b_3 is 2 and 4, for in-plane and cross-plane diffusion, respectively. The values of those parameters are based on the numerical analysis results considering the randomly prescribed pore-filling water distribution, and can be used in the analysis of fuel cell system with a carbon fibre diffusion layer [16,17].

In the present work, the well-known Carman–Kozeny equation supported by experiments [19,20] is applied to describe the relationship of the porosity and the permeability for an individual phase flow. We assume that the permeability of the gas phase gives the following relation with the phase saturation:

$$K^{g}_{eff} = K^{g}_{0}\frac{\bar{\phi}^{3}}{\left(1-\bar{\phi}\right)^{2}}(1-s)^{2} \tag{19}$$

for in-plane permeability, and

$$K^{g}_{eff} = K^{g}_{0}\frac{\bar{\phi}^{3}}{\left(1-\bar{\phi}\right)^{2}}(1-s)^{4} \tag{20}$$

for cross-plane permeability. The assumption of the relationship of the efficient gas permeability and liquid water saturation is based on the research work of Chen et al. [21] and Schulz et al. [22], and the effect of liquid water saturation on the efficient gas diffusivity [16].

The permeability of the liquid water phase is usually described by a power function of its saturation, with an exponent ranging from 1 to 3 [23]. Most of the literatures use 1.5 and 3 in the simulation of PEMFC. The present paper takes it as 1.5, and gives the following expression for the permeability of the liquid water phase:

$$K^{\mathrm{l}}_{\mathrm{eff}} = K^{\mathrm{l}}_0 \frac{\bar{\phi}^3}{\left(1-\bar{\phi}\right)^2} s^{1.5} \tag{21}$$

Although the Carman–Kozeny equation has some limitations to predict the permeability of carbon papers, many researchers show that Carman–Kozeny equation is still applicable if the Carman–Kozeny constant, K^{l}_0, is redefined or treated as an empirical constant based on the experimental results [19,24,25]. Rodriguez's experimental observations [19] showed that the Carman–Kozeny equation can well describe the permeability of the fibre mats (similar to a carbon paper) when the porosity ranges from 0.5 to 0.8. At the present work, the porosity ranges from 0.54 to 0.7, giving a reasonable range to use the Carman–Kozeny equation.

2.4. Unsaturated flow theory (UFT)

Unsaturated flow theory has been widely used in the modeling of fuel cells [3,26]. The pressure in the liquid phase is given by:

$$P^{\mathrm{l}} = P^{\mathrm{g}} - P^{\mathrm{c}} \tag{22}$$

where P^{c} is the capillary pressure. Eqs. (9) and (22) are combined to yield:

$$\begin{aligned} v^{\mathrm{l}} &= -\frac{K^{\mathrm{l}}_{\mathrm{eff}}}{\mu^{\mathrm{l}}}\nabla P^{\mathrm{g}} + \frac{K^{\mathrm{l}}_{\mathrm{eff}}}{\mu^{\mathrm{l}}}\nabla P^{\mathrm{c}} \\ &= -\frac{K^{\mathrm{l}}_{\mathrm{eff}}}{\mu^{\mathrm{l}}}\frac{\mu^{\mathrm{g}}}{K^{\mathrm{g}}_{\mathrm{eff}}}\frac{K^{\mathrm{g}}_{\mathrm{eff}}}{\mu^{\mathrm{g}}}\nabla P^{\mathrm{g}} + \frac{K^{\mathrm{l}}_{\mathrm{eff}}}{\mu^{\mathrm{l}}}\frac{\partial P^{\mathrm{c}}}{\partial s}\nabla s \end{aligned} \tag{23}$$

The capillary pressure between the gas and liquid phases is related to the saturation of liquid phase [27]:

$$P^{\mathrm{c}} = \sigma\,\cos(\theta_{\mathrm{c}})\left(\frac{\bar{\phi}}{K^{l}}\right)^{1/2} J(s) \tag{24}$$

where $J(s)$ is the Leverett function, σ the surface tension for liquid water and air system, θ_{c} the contact angle of the GDL surface. For a hydrophobic GDL [28],

$$J(s) = 1.417s - 2.120s^2 + 1.263s^3 \tag{25}$$

Making use of Eqs. (19)–(21), and (23)–(25), one obtains:

$$\begin{aligned} v^{\mathrm{l}} = {} & \frac{K^{\mathrm{l}}_0}{\mu^{\mathrm{l}}}\frac{\mu^{\mathrm{g}}}{K^{\mathrm{g}}_0}\frac{s^{1.5}}{(1-s)^n}v^{\mathrm{g}} + \frac{\sigma\,\cos(\theta_{\mathrm{c}})(K^{\mathrm{l}}_0)^{1/2}}{\mu^{\mathrm{l}}}\frac{\phi^2}{1-\phi}s^{1.5} \\ & \times(1.417 - 4.24s + 3.78s^2)\nabla s \end{aligned} \tag{26}$$

where n is 2 and 4 for in-plane and cross-plane permeability, respectively, which has been introduced in Eqs. (19) and (20). In this study, the gas and liquid phases within the GDL exist as continuous phases, as a result that the Darcy' law is used to solve the transport phenomena of gas and liquid water, respectively. Eqs. (21) and (23)–(25) come from the literatures of Wang and co-workers [26–28] and Nguyen and co-workers [3].

2.5. Calculation of fuel cell voltage

The polarization curve of a PEM fuel cell plays an important role in determining the performance of the fuel cell system. Due to the irreversible energy loss in a practical fuel cell, the actual potential (V) is decreased from its open circuit voltage (E). These losses include activation overpotential (ΔV_{act}), Ohmic overpotential (ΔV_{ohm}), and concentration overpotential (ΔV_{conc}). Therefore, the operational voltage is [29]:

$$V = E - \Delta V_{\mathrm{ohm}} - \Delta V_{\mathrm{act}} - \Delta V_{\mathrm{conc}} \tag{27}$$

The open circuit voltage, E, is decreased from its thermodynamic potential due to gas crossover. The Ohmic overpotential due to the resistance of the membrane and ions in the cell components (only the membrane resistance and contact resistance are considered here) is given by [29]:

$$\Delta V_{\mathrm{ohm}} = I\,(R_{\mathrm{CR}} + R_{\mathrm{memb}}) \tag{28}$$

where R_{CR} is the contact resistance between the GDL and the bipolar plate, and R_{memb} is the flow resistance of H^+ ions in the electrolyte membrane. The activation overpotential is given by the Tafel equation, which is a transformation of Eq. (17). Concentration overpotential is given as a function of the limiting current in the following form [29]:

$$\Delta V_{\mathrm{conc}} = \frac{RT}{nF}\ln\left(1 - \frac{I}{I_{\mathrm{lim}}}\right) \tag{29}$$

where I_{lim} is the limiting current density. In reality, however, the assumption of a completely mass-transfer limiting case is rarely valid because there is a concentration dependence in the activation kinetics of reaction that affects activation polarization as well [30]. Thus it is neglected at the present simulation.

2.6. Solution strategy

The governing equations of two-phase flow model described in Section 2.3 are discretized using a finite volume staggered scheme. The code is designed using Fortran Language. The well-known SIMPLE algorithm and upwind scheme are utilized in the numerical solution. The studied domain is divided into rectangle elements with four nodes. Finite element analysis for the elastic deformation of the GDL is first carried out to obtain the real shape of the GDL after deformation. The new grid is changed into the approximate orthogonal curvilinear grid. This is helpful to the discretization of the governing equations as described in Section 2.3.

The effect of the number of elements on the computational results is investigated. Numerical tests show that 1600 (20 in

the height and 80 in the length) elements provide a sufficient solution accuracy, giving a good agreement with the numerical result of the rigid GDL [16]. Our numerical solution gives a very good numerical stability, but never meet a convergence problem.

3. Numerical results and discussions

The operating and design parameters used in the present simulation are listed in Table 2. The distributions of the oxygen mole concentration and the liquid water saturation with different clamping pressures are shown in Fig. 3. Effect of the clamping pressure on the performance of the fuel cell is considerable large based on our numerical analysis. To the best of our knowledge, however, no literatures are reported before to consider the deformation of gas diffusion layer caused by the clamping force. The porosity and thickness of the GDL are decreased due to the compression generated by the clamping force. The transport resistance increases with decreasing diffusion and permeability coefficients depending on the GDL porosity. Fig. 3a and Fig. 3b display the distributions of the oxygen mole fraction and the saturation level without considering the elastic deformation of the GDL, but Fig. 3c and Fig. 3d show the different distributions when the elastic deformation of GDL is considered. Obviously, there is a high saturation of liquid water near the interface of the catalyst-layer and the GDL below the inlet due to the GDL deformation (see Fig. 3d). This high saturation is caused by the low transport speed of the gas phase. The friction drag force on the interface of the gas and liquid is helpful to the removal of the liquid water. The saturation of the liquid water leads to a small effective reaction area. The local current density distributions corresponding to Fig. 3 are shown in Fig. 4 for an elastic GDL and a rigid GDL, respectively, when the nominal clamping pressure is 1.93 MPa (the maximum normal deformation of GDL is 0.0753 mm). The average current density considering the GDL elastic deformation is less than half of the current density without considering the GDL deformation (rigid DGL). This is the reason why we should pay more attention to the GDL deformation caused by the clamping force. In fact, the

Table 2
The basic parameters used in the numerical analysis

Parameter	Value
Inlet channel width (half)[a]	0.50 mm
Shoulder width[a]	1.00 mm
Round radius of shoulder angle[b]	0.05 mm
Outlet channel width (half)[a]	0.50 mm
Electrode height[a]	0.25 mm
Membrane thickness (Nafion 112)[c]	0.051 mm
Gas permeability of the electrode, K_0^{g}[b]	1.0×10^{-12} m^2
Liquid-water permeability of the electrode, K_0^{l}[b]	1.0×10^{-12} m^2
Dry porosity of the electrode, ϕ_0[b]	0.7
Inlet mol fraction of oxygen	0.21
Inlet mol fraction of water	0.00
Inlet mol fraction of nitrogen	0.79
Inlet channel pressure[a]	1.007 atm
Outlet channel pressure[a]	1.0 atm
Temperature[a]	60 °C
Gas viscosity, μ^{g}[c]	2.059×10^{-5} Pa s (60 °C)
D^{O} (at T_r)[a]	1.775×10^{-5} m^2 s^{-1} (0 °C)
D^{w} (at T_y)[a]	2.56×10^{-5} m^2 s^{-1} (34 °C)
Condensation rate constant, k_c[a]	100 s^{-1}
Vapourization rate constant, k_v[a]	100 atm^{-1} s^{-1}
Net water transport coefficient, α[a]	0.5
$\sigma \cos(\theta_c)$[b]	-0.0001 N m^{-1}
Liquid-water viscosity, μ^{l}	4.7×10^{-4} Pa s (60 °C)
Proton conductivity of membrane, σ_m[c]	10 Ω^{-1} m^{-1}

[a] Reference [3].
[b] Assumed.
[c] Reference [31].

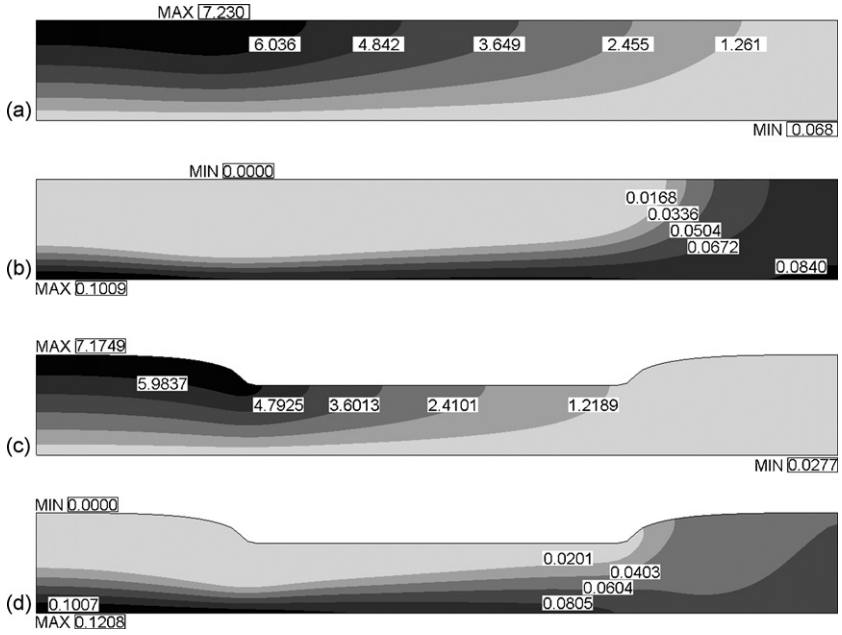

Fig. 3. Comparison of oxygen and water distribution of the fuel cell: (a) the oxygen mole concentration and (b) the saturation level of the liquid water without considering the GDL deformation; (c) the oxygen mole concentration and (d) the saturation level of the liquid water considering the GDL deformation.

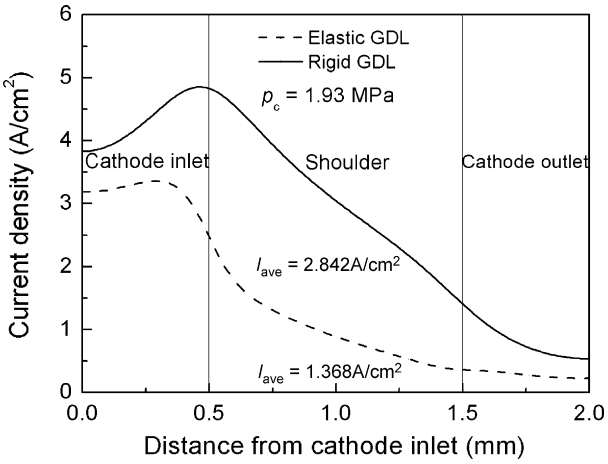

Fig. 4. Current density distribution along the catalyst-layer/GDL interface in the cathode-length direction for the elastic gas diffusion layer (dashed line) and the rigid gas diffusion layer (solid line). The nominal clamping compression p_c = 1.93 MPa.

GDL deformation leads to the change of GDL thickness, except for the change of porosity distribution. The performance of the fuel cell with the interdigitated flow field is sensitive to the GDL thickness [3]. Grujicic and Chittajallu [16] made an optimization for the PEMFC cathode geometrical parameters and concluded that there is an optimum thickness of GDL.

The polarization curves considering different potential losses are plotted in Fig. 5. In the region of Ohmic polarization, the potentials due to the different contact resistances for the graphite and stainless steel shoulders are completely different. When the nominal clamping pressure is 1.93 MPa, the Ohmic resistance of the membrane, the contact resistances with the graphite and stainless steel shoulders are 2.54, 0.252 and 5.2 mΩ m, respectively. The clamping force is an important parameter to control the Ohmic loss for the shoulder having the contact resistivity with the carbon paper as described in case B in Table 1, for example, the stainless steel bipolar plate. However, for the other types of shoulders having a small contact resistance with the carbon paper as described in case A in Table 1, for example the

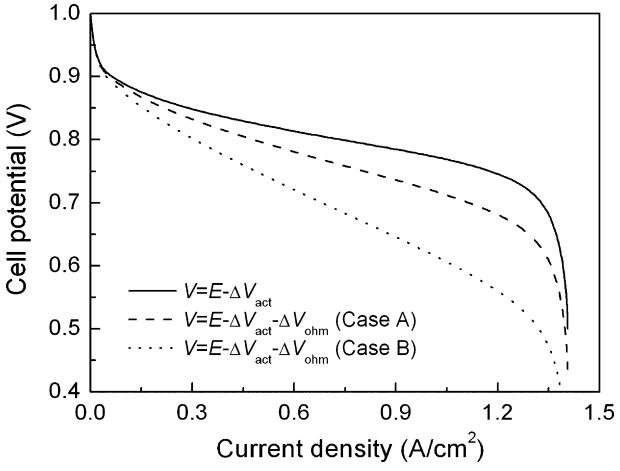

Fig. 5. Polarization curves of the two-phase flow prediction with different shoulder materials of the bipolar plates.

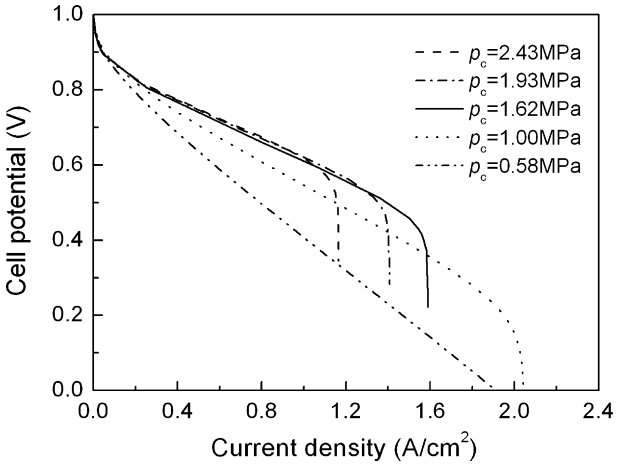

Fig. 6. Polarization curves for different nominal clamping pressures.

graphite bipolar plate, too large a clamping force is not expected due to the higher transport resistance.

Comparisons of the potential and power density of the fuel cell are given in Figs. 6 and 7 for the several clamping pressures as indicated. Effects of the nominal clamping pressure on the interfacial contact resistance and porosity are in two opposite ways: a high clamping force can give a low interfacial contact resistance as expected, but also gives rise to a low porosity of the GDL, which may decrease the system efficiency. For a high contact resistivity shoulder, the contact resistance plays a dominant role due to its large contact resistance at a low clamping force. But at a high clamping force, the contact resistance of this kind of shoulder and carbon GDL decreases slightly with the clamping force. This time the GDL deformation plays a dominant role in determining the power density. However, when the shoulder with a low contact resistivity is used, the GDL deformation is an important factor due to the small contact resistance. Based on the analysis above, we can see that there must exit an optimum clamping force for a practical fuel cell system. The power density decreases with increasing the clamping force when the influence of Ohmic contact resistance is smaller than that of the GDL porosity.

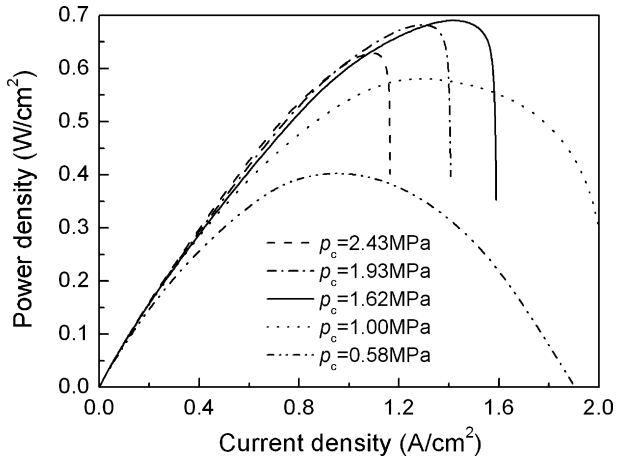

Fig. 7. Power density vs. current density for different nominal clamping pressures.

At the small clamping pressures, what are shown in Figs. 6 and 7 are quantitatively in good agreement with the experimental measurements [32] for a micro-PEMFC with the interdigitated flow field. Unfortunately, at the high clamping pressures, we do not have any experimental data available to compare for the PEMFC with the interdigitated flow field. But good qualitative agreements occur at the polarization and power density curves predicted by the present paper for the interdigitated flow field and by Chu et al. [9] for the one-dimensional model if the porosity change is considered, especially at the high current region. We can estimate that the clamping pressure affects the performance of the PEMFC in a similar manner for any types of flow fields. For the interdigitated flow field, the effect may be larger than the other types of flow fields based on its working mechanism. But this needs a further study. Lee et al. [7] measured the performances of PEMFCs with a serpentine flow field for three types of GDLs (ELAT®, TORAY™, a combination of TORAY™ and CARBEL®) and found that the optimal clamping force is different for different GDLs. However, the changing fashions of the polarization and power density curves are in good agreement with what is predicted in the present paper.

The current density corresponding the maximum power density in the power density-current curve depends on the slope of the polarization curve in the Ohmic region, as shown in Figs. 6 and 7. The slope is controlled by the Ohmic loss and the mass-transport resistance which are affected, respectively, by the contact resistance and the increased transport resistance of reactant caused by the clamping force.

4. Conclusions

Finite element method (FEM) and two-phase flow model are used to investigate the effect of the GDL deformation caused by the clamping force on the performance of an air cathode of the PEM fuel cell with the interdigitated gas distributors. From the numerical results, the following conclusions are reached:

(1) The clamping force affects the permeability and diffusion of the reactant gas and the transport of the liquid water due to the GDL deformation and the porosity variation. A low clamping force increases the interfacial electrical resistance, but a high clamping force decreases the GDL porosity and thus increases the transport resistance of the gas and liquid water.
(2) For a practical fuel cell system, there would be a maximum power density if an optimal clamping force is found. The optimal design parameters for a real fuel cell system depends on the mechanical and electrical properties of the bipolar plates and gas diffusion layer, and the interfacial electrical property and the across shape of the bipolar plates, etc.

Acknowledgments

This research was jointly sponsored by the NSFC (10421002, 10332010), National Basic Research Program of China (2006CB601205), and the Science Research Foundation of Liaoning Province, China (20052178).

References

[1] D.L. Wood, J.S. Yi, T.V. Nguyen, Electrochim. Acta 43 (1998) 3795–3809.
[2] J.S. Yi, T.V. Nguyen, J. Electrochem. Soc. 146 (1999) 38–45.
[3] W. He, J.S. Yi, T.V. Nguyen, AIChE J. 46 (2000) 2053–2064.
[4] L.B. Wang, N.I. Wakayama, T. Okada, Electrochem. Commun. 4 (2002) 584–588.
[5] L.B. Wang, N.I. Wakayama, T. Okada, IAIJ Intl. 45 (2005) 1005–1013.
[6] P. Zhou, C.W. Wu, G.J. Ma, J. Power Sources 159 (2006) 1115–1122.
[7] W.K. Lee, C.H. Ho, J.W. Van Zee, M. Murthy, J. Power Sources 84 (1999) 45–51.
[8] R. Roshandel, B. Farhanieh, E. Saievar-Iranizad, Renew. Energy 30 (2005) 1557–1572.
[9] H.S. Chu, C. Yeh, F. Chen, J. Power Sources 123 (2003) 1–9.
[10] Y. Tang, A.M. Karlsson, M.H. Santare, M. Gilbert, S. Cleghorn, W.B. Johnson, Mater. Sci. Eng. A 425 (2006) 297–304.
[11] V. Mishra, F. Yang, R. Pitchumani, J. Fuel Cell Sci. Technol. 1 (2004) 613–619.
[12] O.C. Zienkiewicz, R.L. Taylor, The Finite Element Method, fifth ed., Butterworth-Heinemann, Oxford, UK, 2000.
[13] J.P. Zheng, J. Power Sources 137 (2004) 158–162.
[14] H. Wang, M.A. Sweikart, J.A. Turner, J. Power Sources 115 (2003) 243–251.
[15] G.L. Batch, S. Cumiskey, C.W. Macosko, Polym. Compos. 23 (2002) 307–318.
[16] M. Grujicic, K.M. Chittajallu, Chem. Eng. Sci. 59 (2004) 5883–5895.
[17] M.M. Tomadakis, S.V. Sotirchos, AIChE J. 39 (1993) 397–412.
[18] J.H. Nam, M. Kaviany, Intl. J. Heat Mass Transf. 46 (2003) 4595–4611.
[19] E. Rodriguez, F. Giacomelli, A. Vazquez, J. Comp. Mater. 38 (2004) 259–268.
[20] G. Mavko, A. Nur, Geophysics 62 (1997) 1480–1482.
[21] C.Y. Chen, R.N. Home, M. Fourar, Water Resour. Res. 40 (2004) W08301.
[22] V. Schulz, D. Kehrwald, A. Wiemann, K. Steiner, NAFEMS Seminar: Simulation of Complex Flows, April 2005.
[23] B. Markicevic, N. Djilali, Phys. Fluids 18 (2006) 033101.
[24] R.C. Lam, J.L. Kardos, ANTEC (1989) 1408–1412.
[25] B.Y. Kim, G.J. Nam, H.S. Ryu, J.W. Lee, Korea-Australia Rheol. J. 12 (2000) 83–92.
[26] U. Pasaogullari, C.-Y. Wang, Electrochim. Acta 49 (2004) 4359–4369.
[27] C.Y. Wang, P. Cheng, Adv. Heat Transf. 30 (1997) 93–196.
[28] U. Pasaogullari, C.Y. Wang, J. Electrochem. Soc. 151 (2004) A399–A406.
[29] EG & G Technical Services, Inc., Fuel Cell Handbook, seventh ed., National Energy Technology Laboratory, West Virginia, 2004, pp. 2-11–2-18.
[30] M.M. Mench, C.Y. Wang, J. Transport Phenomena 3 (2001) 151–176.
[31] Y. Wang, C.Y. Wang, Electrochim. Acta 50 (2005) 1307–1315.
[32] S.S. Hsieh, S.H. Yang, J.K. Kuo, C.F. Huang, H.H. Tsai, Energy Convers. Manage. 47 (2006) 1868–1878.